

Doubly resonant coherent excitation in the x-ray regime: $1s$ - $3d$ transition in H-like Ar¹⁷⁺Alena Ananyeva,^{1,*} Angela Bräuning-Demian,² Yuji Nakano^{3,4,†}, Ken-ichiro Komaki⁴, Yoichi Nakai⁵, Yoko Shiina³, Eiichi Takada,⁶ Takashi Murakami⁶, Alexey V. Stysin⁷, and Toshiyuki Azuma^{4,‡}¹*Department of Physics, Goethe-Universität, 60323 Frankfurt am Main, Germany*²*GSI Helmholtzzentrum für Schwerionenforschung, 64291 Darmstadt, Germany*³*Department of Physics, Rikkyo University, Tokyo 171-8501, Japan*⁴*Atomic, Molecular and Optical Physics Laboratory, RIKEN, Saitama 351-0198, Japan*⁵*RIKEN Nishina Center, Saitama 351-0198, Japan*⁶*National Institutes for Quantum Science and Technology, Chiba 263-8555, Japan*⁷*Skobel'syn Institute of Nuclear Physics, Lomonosov Moscow State University, Moscow 119991, Russia*

(Received 28 November 2023; revised 29 February 2024; accepted 28 March 2024; published 2 May 2024)

The $3d$ states in the $n = 3$ level of H-like Ar¹⁷⁺ ions, to which direct excitation from the $1s$ ground state is optically forbidden, were prepared by the ladder-type ($1s_{1/2} \rightarrow 2p_{3/2} \rightarrow 3d$) double excitation with three-dimensional resonant coherent excitation (3D-RCE). 455 and 390 MeV/u Ar¹⁷⁺ ions were excited by a combination of two different crystal fields induced by the arrangement of crystal planes as they passed through a 1.0- μm -thick Si crystal. We observed resonance profiles in the charge-state distribution of the ions after passing through the thin crystal and in yields of Lyman α and β x rays. The $2p_{3/2} \rightarrow 3d$ transitions were confirmed by depletion of the Lyman α x-ray yield. The observed resonance profile and its dependence on the polarization of the crystal field are in reasonable agreement with theoretical simulations based on the density matrix approach. These results pave the way for the formation of highly excited states of highly charged heavy ions, where the direct transition from the $1s$ ground state is optically forbidden.

DOI: [10.1103/PhysRevA.109.053101](https://doi.org/10.1103/PhysRevA.109.053101)**I. INTRODUCTION**

Population control of highly charged, heavy atomic ions has long been out of reach due to the lack of energy-tunable light sources in the x-ray region. However, with the development of high-energy synchrotron radiation facilities and free-electron lasers, monoenergetic x rays can be produced for resonant excitation of highly charged ions (see Ref. [1] and references therein). Applications to coherent control and pump-probe experiments using two colors in the ultraviolet (UV) and the x-ray regions have also made rapid progress by employing two separate ensembles of electrons at different energies or by two undulator beamlines with different strengths [2–5]. What is more, the future gamma-ray factory at CERN is an ambitious proposal for laser excitation of relativistic heavy ions with only one or a few bound electrons using the relativistic Doppler effect [6]. The approach using resonant coherent excitation (RCE) and heavy ion accelerators allows such observations by choosing the right combination of projectile energy and crystal spacing. It is also possible to observe the charge states of the ions and the resulting electron emission, which is usually difficult with ion traps. In the future, it is expected to target a variety of ion species, such as H-like uranium and unstable RI ions.

RCE in the x-ray region using a periodic crystal field instead of an oscillating field, i.e., real photons, has shown over several decades the excellent ability to control populations of H-like or He-like heavy ions [7–13]. Fast ions passing through a crystal target may undergo transitions between two electronic states if the frequency corresponding to the periodic crystal field sensed by the ions matches their transition energies [14,15]. In 1998, by using highly energetic heavy ions, Komaki *et al.* observed sharp and intense resonances of $1s \rightarrow 2p_{1/2,3/2}$ for H-like Ar¹⁷⁺ ions passing through a Si crystal under the planar channeling condition, which are caused by the crystal field originating from the periodic *atomic string* arrangement, i.e., two-dimensional resonant coherent excitation (2D-RCE) [7,8]. After this observation, Kondo *et al.* found the three-dimensional resonant coherent excitation (3D-RCE) under nonchanneling conditions [9]. Ions penetrating a crystal in arbitrary directions feel the oscillating crystal field originating from the arrangement of the periodic *atomic planes*. Electronic transitions via 3D-RCE can be treated as optical dipole transitions. The ions experience a linearly polarized oscillating field, leading to the alignment of the excited states [10]. Using 3D-RCE opened up a variety of applications, with double resonance (DR) being one typical example.

The Λ -type double resonance ($1s^2 \rightarrow 1s2p \leftrightarrow 1s2s$) using two different frequency components of a single crystal equivalent to photons in the x-ray and vacuum ultraviolet (VUV) regions (3940 and 15 eV, respectively) was demonstrated in He-like Ar¹⁶⁺ ions [11]. The Autler-Townes doublet, a feature of this resonance profile, could be explained by the

*Present address: LIGO, California Institute of Technology, Pasadena, CA 91125, USA.

†nakano@rikkyo.ac.jp

‡toshiyuki-azuma@riken.jp

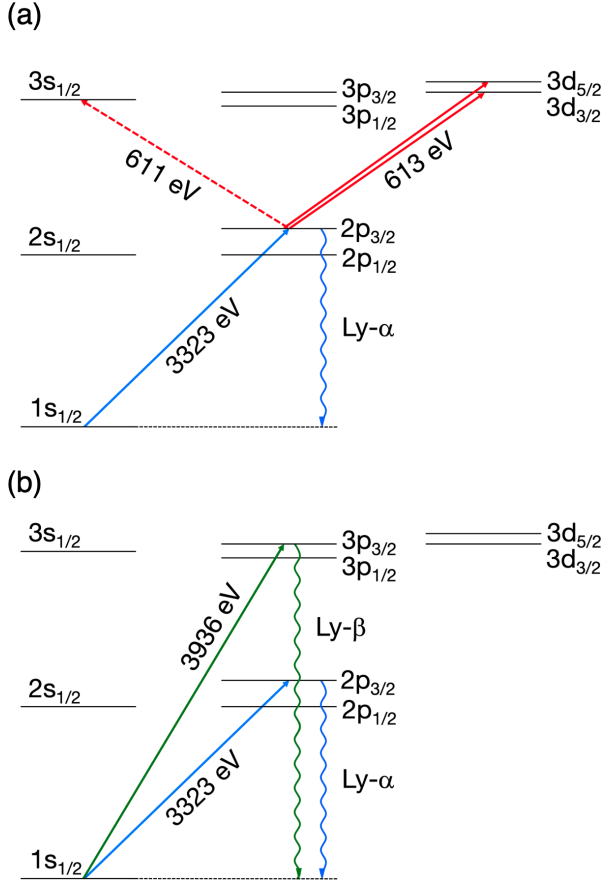


FIG. 1. Schematic energy diagram of (a) ladder-type and (b) V-type double resonances (DR) of Ar^{17+} . Note that both (a) and (b) occur within the resonance width. See the text for details.

dressed-atom concept of quantum optics. Subsequently, the ladder-type resonances ($1s^2 \rightarrow 1s2p \rightarrow 2p^2$) due to two crystal fields equivalent to photons in the x-ray region (3140 and 3287 eV) forming doubly excited states of He-like heavy ions were also confirmed by observation of Auger electrons from the doubly excited state [12].

This method is expected to be a versatile means for accessing unexplored highly excited states of heavy ions, where direct transition from the ground state is dipole forbidden. In this paper, we report on the preparation of $3d$ states of H-like Ar^{17+} ions by the ladder-type resonance ($1s \rightarrow 2p \rightarrow 3d$) with two different crystal fields equivalent to photons in the x-ray region (3323 eV and 613 eV). A schematic energy diagram of the ladder-type three-state configuration is shown in Fig. 1(a), and the corresponding energies of the states are listed in Table I. The total oscillator strengths, i.e., the oscillator strengths multiplied by the statistical weights of the initial and final states of $2p_{3/2} \rightarrow 3s_{1/2}$, $3d_{3/2}$, $3d_{5/2}$ for hydrogen, have been calculated theoretically to be 0.05, 0.28 and 2.50, respectively [16]. Their ratio is similar for H-like heavy ions, with the transition $2p_{3/2} \rightarrow 3d_{5/2}$ being the primary channel, followed by $2p_{3/2} \rightarrow 3d_{3/2}$, and $2p_{3/2} \rightarrow 3s_{1/2}$ being negligibly small. The calculated oscillator strengths of the relevant transitions [17] are given in Table II. First the $1s_{1/2}$ electron is excited to the $2p_{3/2}$ state and subsequently the $2p_{3/2}$ electron is excited to the $3s$, $3d$ states, where $3d_{5/2}$ is the dominant final

TABLE I. Transition energy of the excited states from the $1s_{1/2}$ ground state in Ar^{17+} [18].

State	Energy (eV)
$2p_{1/2}$	3318.17737
$2p_{3/2}$	3322.993290
$3s_{1/2}$	3934.34189
$3p_{1/2}$	3934.29458
$3p_{3/2}$	3935.72192
$3d_{3/2}$	3935.719420
$3d_{5/2}$	3936.191400

state. In the following, we reveal these dynamics through an elaborate combination of different experimental approaches and theoretical simulations.

II. THEORETICAL BACKGROUND

A. RCE and DR

The periodic electric field in a crystal is generally represented in a Fourier series of reciprocal lattice vectors \mathbf{g} as

$$\mathbf{F}(\mathbf{r}) = \sum_{\mathbf{g}} \mathbf{F}_{\mathbf{g}} \exp(-2\pi i \mathbf{g} \cdot \mathbf{r}), \quad (1)$$

with $\mathbf{F}_{\mathbf{g}} = 2\pi \mathbf{g} V_{\mathbf{g}}$, $V_{\mathbf{g}}$ being the Fourier coefficient of the scalar potential. Here, the direction of $\mathbf{F}_{\mathbf{g}}$ is parallel to \mathbf{g} , i.e., normal to the corresponding atomic planes. In the rest frame of traveling ions, ions with a velocity vector \mathbf{v} feel the crystal field \mathbf{F}' consisting of different oscillating fields of frequency $\nu_{\mathbf{g}}$ generated by the arrangement of atomic planes specified by the reciprocal lattice vector \mathbf{g} :

$$\mathbf{F}'(t') = \sum_{\mathbf{g}} \mathbf{F}'_{\mathbf{g}} \exp(-2\pi i \nu_{\mathbf{g}} t'), \quad (2)$$

$$\nu_{\mathbf{g}} = \gamma \mathbf{v} \cdot \mathbf{g}, \quad (3)$$

where γ is the Lorentz factor. The resonance condition for the transition energy E_{trans} of the ions is given by

$$E_{\text{trans}} = h\nu_{\mathbf{g}}, \quad (4)$$

where h is Planck's constant [9].

A Si crystal was employed as a target. As described in Ref. [10], the orientation of the crystal with respect to the ion beam is defined by the angles θ and ϕ , as shown in Fig. 2(a). The laboratory frame of reference was defined as follows: the z axis is taken to be parallel to the ion beam direction, and the x axis to be upward vertically. A new set of the base lattice vectors in the diamond structure was chosen as

TABLE II. Oscillator strength of the relevant transitions of Ar^{17+} [17].

Transition	Oscillator strength
$1s_{1/2} \rightarrow 2p_{3/2}$	0.27337
$1s_{1/2} \rightarrow 3p_{1/2}$	0.026067
$1s_{1/2} \rightarrow 3p_{3/2}$	0.052143
$2p_{3/2} \rightarrow 3s_{1/2}$	0.014278
$2p_{3/2} \rightarrow 3d_{3/2}$	0.069389
$2p_{3/2} \rightarrow 3d_{5/2}$	0.62379

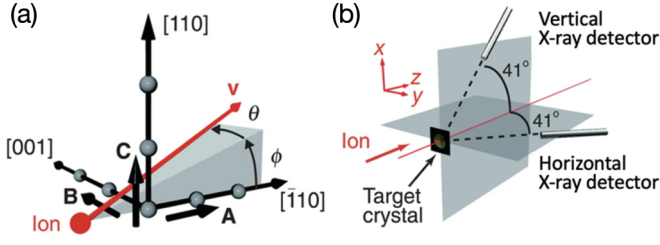


FIG. 2. (a) Orthogonal coordinate system for a Si crystal. The red arrow represents the velocity vector \mathbf{v} of the ion penetrating the crystal, and θ and ϕ are the ion incident angles with respect to the $[110]$ axis. (b) Schematic measurement geometry. Two semiconductor x-ray detectors were installed in the horizontal and vertical planes. The target crystal was mounted on a high-precision three-axis goniometer [10].

$\mathbf{A} = (-1, 1, 0)a/2$, $\mathbf{B} = (0, 0, 1)a$, and $\mathbf{C} = (1, 1, 0)a/2$, a being the lattice constant. The target crystal was mounted on a goniometer so that the directions of the x , y , and z axes and those of the lattice vectors, \mathbf{C} , $-\mathbf{B}$, and \mathbf{A} coincide, respectively, when $\theta = \phi = 0$. Introducing a new Miller index (k, l, m) for the new basis, the reciprocal lattice vector is represented as $\mathbf{g}_{k,l,m} = k\mathbf{A}^* + l\mathbf{B}^* + m\mathbf{C}^*$, where $\mathbf{A}^* = (-1, 1, 0)/a$, $\mathbf{B}^* = (0, 0, 1)/a$, $\mathbf{C}^* = (1, 1, 0)/a$ are the bases of the reciprocal lattice space. The resonance condition for the transition energy E_{trans} for the crystal field with $\mathbf{g}_{k,l,m}$ is given by

$$E_{\text{trans}} = E_{k,l,m}(\theta, \phi) = \frac{h\nu\gamma}{a}(\sqrt{2}(k \cos \phi + m \sin \phi) \cos \theta + l \sin \theta), \quad (5)$$

where $v = |\mathbf{v}|$. The resonance conditions of 3D-RCE are satisfied by adjusting the two independent angles θ and ϕ with the ion velocity v fixed. Tilting the crystal with respect to the ion beam corresponds to scanning the oscillating frequency of the crystal field. In this experiment, the angle θ was scanned while keeping ϕ fixed. After 3D-RCE, the excited ions either experience ionization by collisions with crystal atoms or deexcite to their initial state by emitting x rays. The ionization cross section of the excited states is larger than the ground state, and that of the $n = 3$ level is larger than the $n = 2$ level, thus increasing the ionization probability in the crystal.

The resonance profiles were obtained by measuring (i) the charge-state distribution of the ions after passing through the thin crystal target and (ii) the yield of deexcitation x rays emitted from the ions. The anisotropy in the angular distribution of the x-ray emission is due to the excitation of magnetic sub-states by a specific polarization of the oscillating field. It is explained theoretically in the Appendix and calculated by the density matrix approach, which is described in the next subsection.

Each component of the frequency $\nu_{\mathbf{g}}$ shown in Eqs. (2) and (3) corresponds to a specific reciprocal lattice vector of the atomic plane $\mathbf{g}_{k,l,m}$. By definition, when two frequencies of the crystal field are combined, their sum and difference frequencies are naturally present in the crystal field unless the Fourier coefficient of the electric field for the resultant reciprocal lattice vector vanishes due to destructive interference (the extinction rule) [7,19]. Among three states of a ,

b , and c , when two frequencies satisfy resonance conditions for $a \rightarrow b$ (transition energy: $h\nu_{\mathbf{g}_{k_1,l_1,m_1}}$) and $b \rightarrow c$ (transition energy: $h\nu_{\mathbf{g}_{k_2,l_2,m_2}}$) simultaneously, the $a \rightarrow c$ direct transition is always resonated by the component of another frequency at ν corresponding to $\mathbf{g}_{k_1,l_1,m_1} + \mathbf{g}_{k_2,l_2,m_2}$.

In the present study, two different oscillating fields are used for the transition from the $n = 1$ to $n = 2$ level ($1s_{1/2} \rightarrow 2p_{3/2}$), and that from the $n = 2$ to $n = 3$ level ($2p_{3/2} \rightarrow 3d$), leading to ladder-type DR. The ions simultaneously feel the field of their sum frequency corresponding to transitions $1s_{1/2} \rightarrow 3d$, which are optically forbidden. The energy difference among five substates in the $n = 3$ level is below 2 eV, as shown in Table I. These states are not distinguishable in 3D-RCE because the typical resonance width is found to be a few eV full width at half maximum (FWHM) in this experiment. Therefore, the field specified by $\mathbf{g}_{k_1,l_1,m_1} + \mathbf{g}_{k_2,l_2,m_2}$ coincides with the transition from the $n = 1$ to $n = 3$ level ($1s_{1/2} \rightarrow 3p$), and a V-type DR ($1s_{1/2} \rightarrow 2p_{3/2}$, $1s_{1/2} \rightarrow 3p$) is expected as shown in Fig. 1(b) in addition to ladder-type DR.

This is seemingly similar but essentially different from the sum frequency generation (SFG) and difference frequency generation (DFG) in nonlinear optical media, which are based on higher-order processes of real photons induced by intense external laser fields.

B. Density matrix calculation

We performed a numerical simulation of the RCE process using the density matrix approach developed by Balashov *et al.* [20–23]. The simulation takes into account the collisional excitation, ionization, and radiative decay of the ions in the crystal, leading to decoherence, in addition to the coherent excitation by the crystal fields. We traced the time evolution of the populations of specific states of ions moving through the crystal. A total of 28 states were treated corresponding to the $|jm\rangle$ -resolved substates of $n = 1, 2$, and 3 states of Ar^{17+} .

The charge-state distribution at the exit of the crystal is evaluated and compared with experimental data. The x-ray yield is calculated as the sum of emission both in the crystal and in a vacuum after the exit. The observed Lyman α and β ($\text{Ly}\alpha$ and $\text{Ly}\beta$) x rays, with energies above 3 keV, penetrate through the thin Si crystal target. However, the majority of the x-ray emission occurs after passing through the 1.0- μm -thick crystal because the intrinsic lifetime of the excited states is on the order of ~ 10 fs [24] and the excited ions travel more than a hundred μm before x-ray emission. Thus, it is primarily the population of excited states at the exit that determines the observed x-ray intensity.

Cross sections for collisional ionization and excitation from the ground and excited states are provided by the computation code ETACHA4 [25], as listed in Table III. Transitions between the $|jm\rangle$ -resolved substates were evaluated using the algebra of Clebsch-Gordan coefficients by taking into account statistical weights. The ionization cross sections are larger for the higher excited states. Electron capture cross sections are not included in the calculation because they are negligibly small.

The energy width and loss of the incident ion beam are again negligibly small, and therefore, not taken into account. The angular divergence of the incident ions is also not taken

TABLE III. Collisional ionization and excitation cross-sections of Ar^{17+} in a solid Si target [25] used for the calculation of the population evolution of the excited states. The $3s \rightarrow 3p$ cross section is used also for $3s \rightarrow 3d$ and $3p \rightarrow 3d$ excitations.

Transition	Cross section [$\times 10^{-20} \text{cm}^2$]	
	Case I 455.32 MeV/u	Case II 389.82 MeV/u
1s ioni.	2.77	3.01
2s ioni.	10.5	11.4
2p ioni.	11.2	12.3
3s ioni.	25.9	28.3
3p ioni.	25.9	28.3
3d ioni.	25.9	28.3
1s \rightarrow 2s	0.220	0.240
1s \rightarrow 2p	3.07	3.33
1s \rightarrow 3s	0.0446	0.0486
1s \rightarrow 3p	0.569	0.616
1s \rightarrow 3d	0.0318	0.0347
2s \rightarrow 2p	16.5	18.0
2s \rightarrow 3s	1.83	2.00
2s \rightarrow 3p	5.22	5.70
2s \rightarrow 3d	6.24	6.81
2p \rightarrow 3s	0.249	0.271
2p \rightarrow 3p	2.10	2.30
2p \rightarrow 3d	13.6	14.9
3s \rightarrow 3p	25.7	28.0

into account, but its contribution is discussed later for case II. Elastic collisions that change the direction of the ions were not considered.

Finally, it is noted that the crystal field induces ac-Stark mixing and splitting in the energy level. These contributions were taken into account in the calculation; however, they are much smaller than the observed resonance width in the present condition. We clearly observed them for the case of the strong coupling of the relevant states [11].

III. EXPERIMENTS

Ion beams of 455.32 and 389.80 MeV/u Ar^{17+} were produced at the Heavy Ion Medical Accelerator (HIMAC) in Chiba, Japan, with a small angular divergence of less than 0.05 mrad. The incident energy of the ions was evaluated from the peak position of the $1s_{1/2} \rightarrow 2p_{1/2}$ transition in the resonance profile of the $\text{Ly}\alpha$ x-ray emission yield. A schematic layout of the setup is shown in Fig. 3. This is

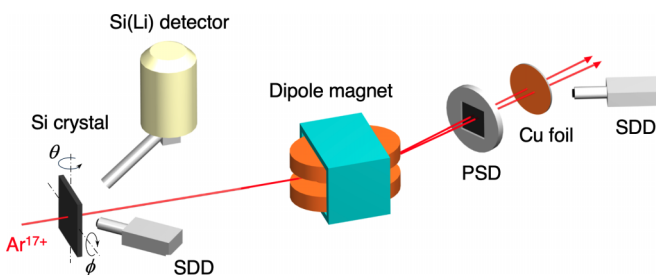


FIG. 3. Schematic layout of the experimental setup.

essentially the same as the previously reported experiments [10]. A beam collimator with a diameter of 0.6 mm and thickness of 50 mm was placed 6.50-m upstream of the target. A 1.0- μm -thick Si crystal target was mounted on a specially designed high-precision three-axis goniometer. The angles of the three rotation axes were controlled by stepping motors coupled with several gears; their precision was assessed (including repeatability) by a combination of the attached reflection mirror and a He-Ne laser. The precision of the θ rotation achieved is better than 0.005° . The geometrical configuration shown in Fig. 2 was fulfilled by placing the target so that the (220) plane is horizontal at $\phi = 0$, and the $[\bar{1}10]$ direction is parallel to the ion beam at $\theta = \phi = 0$.

We performed two types of measurements independently under the conditions of low and high ion intensities. A dipole magnet of 0.5 T at maximum separates ions with different charge states after passing through the crystal target. Under the low-intensity condition for the charge-state measurement, the ions were subsequently detected by a two-dimensional position-sensitive silicon detector (2D-PSD) placed 5.6-m downstream from the crystal target. This detector is a 20 mm \times 20 mm square-shaped PIN diode detector (First Sensor Technology GmbH). The intensity of the ion beam for the charge-state measurements was kept below 5×10^3 ions per pulse with a width of 1 s to avoid counting losses.

Under the high-intensity condition for the x-ray detection, we measured the yield of x rays from the excited states of the Ar^{17+} ions. To study the angular anisotropy of the x-ray emission, two solid-state x-ray detectors were placed at a distance of about 150 mm from the target crystal and at an angle of 41° to the beam direction along the vertical and horizontal planes, respectively, as shown in Fig. 3. Vertical and horizontal detectors are placed on the x - z and y - z planes, which coincide with the (004) plane at $\theta = 0$ and the (220) plane at $\phi = 0$, respectively. In the ion rest frame, the Lorentz transformed detection angle was almost 90° , i.e., in the x' and y' directions. The Si(Li) detector (Princeton Gamma-Tech Instruments Inc.) placed in the vertical direction has an effective thickness of 6 mm and a detection area of 30mm^2 . The silicon drift detector (SDD) (KETEK GmbH) placed in the horizontal direction has an effective thickness of 450 μm and a detection area of 80mm^2 . For evaluating the relative geometrical factor of the two detectors, $\text{Ly}\alpha$ x rays from Ar^{17+} produced by the collisional process at nonresonance conditions were used, assuming their isotropic emission with respect to the beam axis. The energy calibration of the detectors was performed using 5.9 keV x rays from a ^{55}Fe source. The measured energy resolution was 145 and 165 eV for vertical and horizontal detectors, respectively, which is enough to separate $\text{Ly}\alpha$ and $\text{Ly}\beta$ x rays. It is noted that the width of the resonance peaks does not stem from these resolutions.

We needed the projectile intensity for the normalization of the obtained spectrum of x rays from Ar^{17+} . However, the typical ion beam intensity for the x-ray measurement was on the order of 10^6 ions per pulse with a width of 1 s, which cannot be measured in the counting mode by the 2D-PSD. Therefore, we monitored $\text{K}\alpha$ x rays of 8.05 keV emitted from a Cu foil placed on the axis of the projectile by using the additional silicon drift detector (SDD) (KETEK GmbH)

placed 0.5-m away from the Cu foil as shown in Fig. 3, whose energy resolution is around 200 eV.

IV. RESULTS AND DISCUSSION

Before explaining our approach and observed resonance spectra, we define the resonance width, which is critical for the discussion. The resonance widths originate from several factors: relaxation of the coherence between the lower and upper states in the resonance due to the collisions in the crystal, but also from the nonnegligible velocity spread and beam divergence. As already stated, the typical resonance width ΔE is a few eV FWHM as a function of the transition energy, i.e., $\Delta E/E_{\text{trans}}$ is about 10^{-3} , in the present experiment [9].

When scanning the ion incident angle θ , the resonance width in the angular spectrum $\Delta\theta$ depends on the Miller index (k, l, m) of the resonance. Hereafter referred to as the *apparent* resonance width, it differs from the resonance energy width in terms of the transition energy ΔE . It is understood by the derivative of Eq. (5) as follows:

$$\frac{\partial E_{k,l,m}(\theta, \phi)}{\partial \theta} = \frac{h\nu\gamma}{a} (-\sqrt{2}(k \cos \phi + m \sin \phi) \sin \theta + l \cos \theta). \quad (6)$$

In the present experimental condition, ϕ and θ are small. This leads to

$$\frac{\partial E_{k,l,m}(\theta, \phi)}{\partial \theta} \sim \frac{h\nu\gamma}{a} (-\sqrt{2}(k + m\phi)\theta + l). \quad (7)$$

When l is large, it is clear from Eq. (7) that $E_{k,l,m}(\theta, \phi)$ varies to a large extent by changing the angle. ΔE and $\Delta\theta$ are connected by the relation $\Delta\theta = \Delta E/(\partial E_{k,l,m}(\theta, \phi)/\partial \theta)$, leading to narrow $\Delta\theta$.

The *apparent* resonance width $\Delta\theta$ is further convoluted by experimental factors like the velocity (v) spread and beam divergence. $\Delta v/v$ is estimated to be of the order of 10^{-4} , and its contribution is much smaller than $\Delta E/E_{\text{trans}}$. The angular divergence of the beam is estimated to be a few 0.01 mrad, evaluated by the beam profile on the 2D detector and the configuration of the beam transport, and its contribution is again small. However, it depends on the beam transportation condition, which will be mentioned later.

Two approaches were taken to study ladder-type DR or V-type DR under different conditions. One is when all transitions have similar *apparent* resonance widths (case I). The other is when two transitions from the $n = 1$ level have similar *apparent* resonance width, but the transition from the $n = 2$ to the $n = 3$ level has a much narrower width reflecting a large l component of the Miller index (case II). By combining resonances with different *apparent* resonance widths into DR, the processes involved can be clearly identified.

A. Case I: Small l component of the Miller index

An incident energy of 455.32 MeV/u was chosen for the Ar^{17+} ion beam. The resonance condition diagram as a function of angles θ and ϕ was calculated using Eq. (4) with $(k, l, m) = (1, -1, 0)$ for $1s-2p$, $(k, l, m) = (1, 2, 3)$ for $1s-3p$, and $(k, l, m) = (0, 3, 3)$ for $2p_{3/2}-3s, 3d$ transitions.

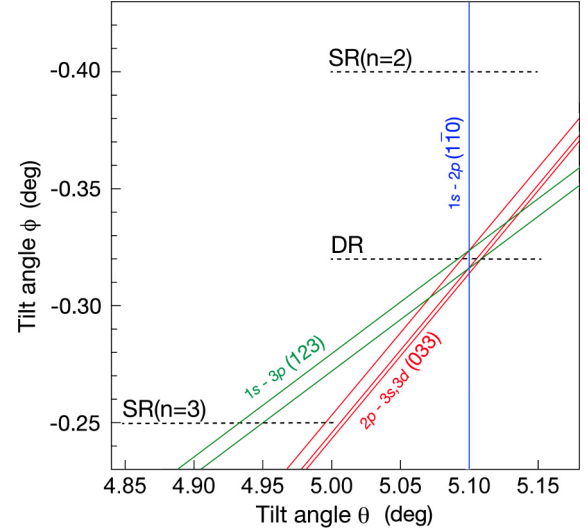


FIG. 4. The 3D-RCE resonance condition diagram of 455.32 MeV/u Ar^{17+} : $1s_{1/2} \rightarrow 2p_{3/2}$ with the field specified by $\mathbf{g}_{1,-1,0}$ (blue line) and $1s_{1/2} \rightarrow 3p_{1/2,3/2}$ by $\mathbf{g}_{1,2,3}$ (green lines), $2p_{3/2} \rightarrow 3s_{1/2}, 3d_{3/2,5/2}$ by $\mathbf{g}_{0,3,3}$ (red lines), respectively. The black dashed lines are the scanned θ regions at fixed ϕ under three conditions: SR($n = 2$), SR($n = 3$), DR.

Figure 4 shows the result in which each point on the line satisfies the corresponding resonance condition. We scanned the angle θ keeping the angle ϕ constant under three different conditions where the *apparent* resonance width does not vary much between the transitions reflecting the low l component. The first scan is for a single resonance SR($n = 2$) profile of the transition of $1s_{1/2} \rightarrow 2p_{3/2}$ by the field specified by $\mathbf{g}_{1,-1,0}$. The second scan is for a single resonance SR($n = 3$) profile of the transition of $1s_{1/2} \rightarrow 3p$ by the field specified by $\mathbf{g}_{1,2,3}$. The third scan is for a double resonance DR profile. As already mentioned, the ladder-type DR of $1s_{1/2} \rightarrow 2p_{3/2} \rightarrow 3d$ is realized in the same condition within the resonance width where the V-type DR of $1s \rightarrow 2p_{3/2}$ and $1s \rightarrow 3p$ occurs. The oscillation frequency specified by the $\mathbf{g}_{0,3,3} = \mathbf{g}_{1,2,3} - \mathbf{g}_{1,-1,0}$ satisfies the resonance condition for the transition of $2p_{3/2} \rightarrow 3s, 3d$ of the ladder-type DR. Figures 5(a), 5(b) and 5(c) show the observed resonance profiles of the Ar^{18+} fraction, the $\text{Ly}\alpha$ x-ray yield, and the $\text{Ly}\beta$ x-ray yield, respectively, under the single resonance SR($n = 2$) of $1s_{1/2} \rightarrow 2p_{3/2}$. As for the charge-state distribution, a fraction of 0.2 of the incoming Ar^{17+} ions appeared as Ar^{18+} as the baseline, after passing through the crystal due to collisions with crystal atoms, while a fraction of 0.8 survived as Ar^{17+} . The Ar^{18+} fraction increased to 0.25 at the peak of the SR($n = 2$) condition, reflecting the larger ionization cross section of the excited states. The $\text{Ly}\alpha$ x-ray yield also increased in both vertical and horizontal directions (0.88 and 0.55, respectively). For the angular anisotropy, the vertical emission is clearly favored, i.e., the vertical to horizontal x-ray yield ($R_{V/H}$) is 1.60. As for the $\text{Ly}\beta$ x-ray yield, the enhancement is negligibly small within the statistical uncertainty.

For SR($n = 3$) profiles, the Ar^{18+} fraction increased to 0.23 [Fig. 5(d)]. While the $\text{Ly}\alpha$ x-ray yield did not increase [Fig. 5(e)], a significant enhancement in the $\text{Ly}\beta$ x-ray yield was observed [Fig. 5(f)]. However, it is roughly ten times

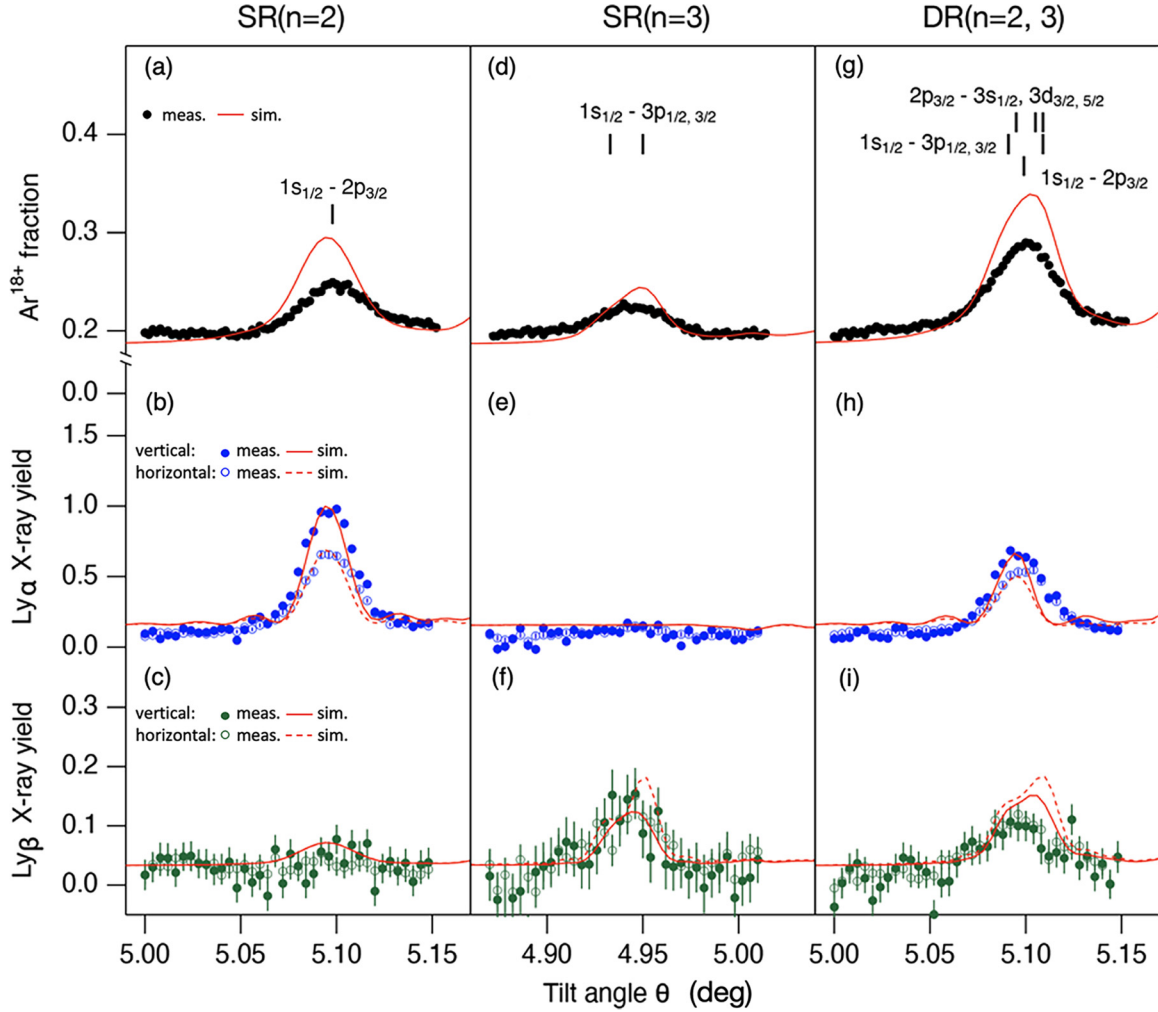


FIG. 5. Resonance profiles as a function of θ for 455.32 MeV/u Ar^{17+} ions. SR($n = 2$) profiles of $1s_{1/2} \rightarrow 2p_{3/2}$ at $\phi = -0.400^\circ$: (a) Ar^{18+} fraction, (b) $\text{Ly}\alpha$ x-ray yield, (c) $\text{Ly}\beta$ x-ray yield. SR($n = 3$) profiles of $1s_{1/2} \rightarrow 3p_{1/2,3/2}$ at $\phi = -0.250^\circ$: (d) Ar^{18+} fraction, (e) $\text{Ly}\alpha$ x-ray yield, (f) $\text{Ly}\beta$ x-ray yield. DR resonance profiles at $\phi = -0.320^\circ$: (g) Ar^{18+} fraction, (h) $\text{Ly}\alpha$ x-ray yield, (i) $\text{Ly}\beta$ x-ray yield. Inserted vertical bars denote the resonance angles calculated from Eq. (5). Filled and open circles in the x-ray yield show measurements by the detectors placed in the vertical and horizontal directions, respectively. They are normalized to the baseline at the SR($n = 2$) condition [Fig. 5(b)]. The red curve overlaid on each profile is the corresponding resonance spectra from the simulation. For x-ray yields, solid and dashed lines show simulated resonance spectra in the vertical and horizontal directions, respectively. They are scaled to match the ones measured at the (b) SR($n = 2$) condition and this common scaling factor is employed for the $\text{Ly}\alpha$ and $\text{Ly}\beta$ x-ray yields.

smaller than the SR($n = 2$) $\text{Ly}\alpha$ x-ray yield [Fig. 5(b)]. This is because collisional ionization is more dominant than x-ray emission, reflecting the ionization cross-sections for the $n = 3$ level being more than twice those for the $n = 2$ level, as shown in Table III. The statistical quality of the $\text{Ly}\beta$ x-ray yield data was insufficient to discuss the angular anisotropy.

We then proceeded to DR. Figure 5(g) shows that the Ar^{18+} fraction at the resonance peak was further enhanced to 0.29. In Figs. 5(h) and 5(i), both $\text{Ly}\alpha$ and $\text{Ly}\beta$ x-ray yields were enhanced, indicating that both the $n = 2$ and 3 levels are populated under DR. At first glance, this behavior can be explained simply by V-type DR, as long as the ground state has a sufficient population. The increase of the Ar^{18+} fraction by 0.09 above the nonresonance condition is close to the sum of the 0.05 and 0.03 increases for SR($n = 2$) and SR($n = 3$), respectively. The enhancement of the $\text{Ly}\beta$ x-ray yield [Fig. 5(i)] is considered to originate from direct RCE to

the $n = 3$ level in the V-type DR, and its intensity is similar to SR($n = 3$) [Fig. 5(f)]. Note that this enhancement is not due to ladder-type DR because it should produce the $3d_{3/2,5/2}$ states, which are not allowed to decay to the ground state by single-photon emission. However, the $\text{Ly}\alpha$ x-ray yield was clearly reduced at the DR condition [Fig. 5(h)] compared to the SR($n = 2$) condition [Fig. 5(b)]; it is reduced by 35% (from 0.88 to 0.57) in the vertical direction and 20% (from 0.55 to 0.44) in the horizontal direction. This reflects the depletion of the $2p_{3/2}$ state population due to population transfer to the $3s_{1/2}$, $3d_{3/2,5/2}$ states in ladder-type DR. The depletion of the $\text{Ly}\alpha$ x rays was more prominent in the vertical direction compared to the horizontal. Considering the polarization of the oscillating field, the vector $\mathbf{F}_{-1,1,0}$ has electric field components in y and z , and thus excites the $2p_y$ and $2p_z$ substates, while $\mathbf{F}_{3,3,0}$ has x and y components [10]. This resulted in selective depletion of the $2p_y$ substate, making $R_{V/H}$ of the

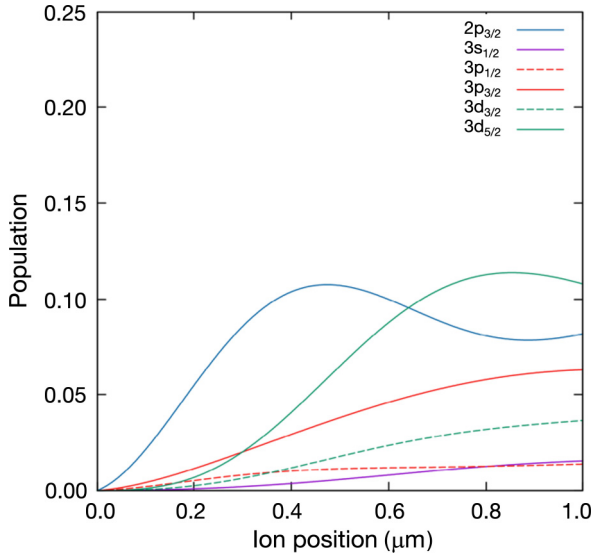


FIG. 6. Calculated population evolution of the excited states of Ar^{17+} as a function of the penetration depth from the entrance in the crystal under the DR condition of $\theta = 5.109^\circ$ and $\phi = 0.320^\circ$ for case I. The population is normalized to the incoming Ar^{17+} ions.

$\text{Ly}\alpha$ x-ray yield in the DR condition smaller than that in the SR condition. To summarize case I, the ladder-type DR was confirmed by the reduction of the $\text{Ly}\alpha$ x-ray yield compared with the case of $\text{SR}(n = 2)$ in addition to V-type DR.

Hereafter, we compare the observed resonance profiles with simulations by the density matrix method. Each of the calculated resonance profiles is overlaid in Fig. 5. Calculated x-ray yields are scaled to match the ones measured at the $\text{SR}(n = 2)$ condition [Fig. 5(b)], and this common scaling factor is employed for the $\text{Ly}\alpha$ and $\text{Ly}\beta$ x-ray yields. The baseline of the Ar^{18+} fraction is well reproduced; however, the increase at the peak of the resonance condition is overestimated. The origin of this is not clear, but larger collisional ionization cross sections employed for the excited states may account for this discrepancy. The simulation reproduced the characteristic behavior of the $\text{Ly}\alpha$ x-ray yield both in the vertical and horizontal directions [Figs. 5(b) and 5(h)]. The calculated anisotropy, i.e., $R_{V/H}$, of 1.59 and 1.46 in the $\text{SR}(n = 2)$ and DR conditions also agrees with our observations. The difference in $R_{V/H}$ is due to the direction of the oscillating field for $2p_{3/2} \rightarrow 3s, 3d$ of the ladder-type DR.

For $\text{Ly}\beta$ x-ray yields, the increase under $\text{SR}(n = 3)$ [Fig. 5(f)] and DR conditions [Fig. 5(i)], including the ratio of the $\text{Ly}\beta$ x-ray yield to the $\text{Ly}\alpha$ x-ray yield, were well reproduced.

To obtain the simulated spectra mentioned above, we calculated the population evolution of each excited state as a function of ion position, i.e., the penetration depth from the entrance surface of the crystal. For a deeper understanding, the case at the peak of the DR condition $\theta = 5.109^\circ$, $\phi = -0.320^\circ$, where the largest population of the $3d_{5/2}$ state is theoretically expected, was shown in Fig. 6. The population in the $2p_{3/2}$ state increases as the ions travel and reaches a maximum at around $0.47 \mu\text{m}$ from the entrance, and then decreases. Accompanied by this enhancement, the population of the $3d_{3/2,5/2}$ states also increases due to population

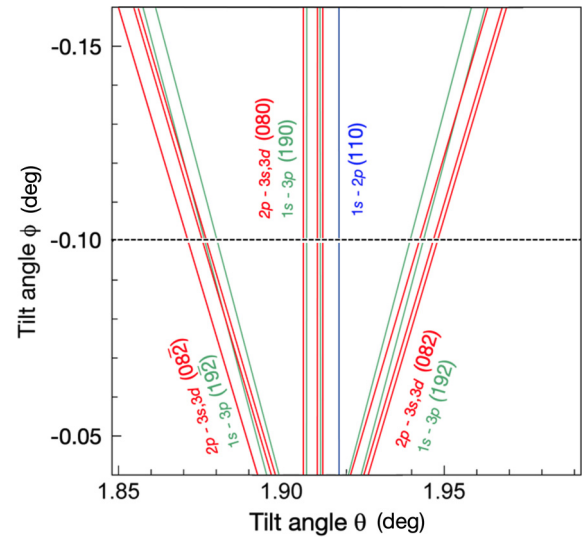


FIG. 7. The 3D-RCE resonance condition diagram of $389.80 \text{ MeV/u Ar}^{17+}$: $1s_{1/2} \rightarrow 2p_{3/2}$ with the field specified by $\mathbf{g}_{1,1,0}$ (blue line), $1s_{1/2} \rightarrow 3p_{1/2,3/2}$ by $\mathbf{g}_{1,9,m}$ (green lines), and $2p_{3/2} \rightarrow 3s_{1/2}, 3d_{3/2,5/2}$ by $\mathbf{g}_{0,8,m}$ (red lines), where $m = 2, 0, -2$. The black dotted line is the scanned θ region for fixed $\phi = -0.100^\circ$ in the measurements.

transfer from the $2p_{3/2}$ state. The increase in population of the $3p_{3/2}$ state is also appreciable. The population ratio of $3d_{5/2}$ to $3d_{3/2}$ is smaller than the value expected from the total oscillator strength (0.62 versus 0.07) shown in Table II. This reflects the contribution of the nonresonant component due to inelastic collisions. That is, the ions are excited by collisions with atoms in the crystal, and the population of excited states gradually increases as the ions penetrate the crystal.

These behaviors indicate that the largest population of the $3d_{5/2}$ state is indeed achieved by the population transfer via ladder-type DR; around 11% of the incoming ions are excited to the $3d_{5/2}$ state. However, the population of $3p_{1/2,3/2}$ states also increases as a result of V-type DR.

B. Case II: Large l component of the Miller index

Using a $389.80 \text{ MeV/u Ar}^{17+}$ ion beam, we excited the $1s_{1/2}$ ground-state electron to the $2p_{3/2}$ state with the field specified by $\mathbf{g}_{1,1,0}$, and further excited it to the $3d_{3/2,5/2}$ states with the field specified by $\mathbf{g}_{0,8,m}$, where $m = 2, 0, -2$. The resonance condition diagram is presented in Fig. 7. In contrast to case I, the second resonance has a much narrower *apparent* resonance width, reflecting the large l component ($l = 8$) of the Miller index. Resonant excitation to the $3p_{1/2,3/2}$ states from the $1s_{1/2}$ ground state with the field specified by the $\mathbf{g}_{1,9,m}$ ($m = 2, 0, -2$) occurs at the same time, as in case I.

The obtained resonance profiles possess a rich structure, as shown in Fig. 8. The Ar^{18+} fraction [Fig. 8(a)] is characterized by a large, broad feature peaking as high as 0.30 above the baseline of 0.20 and centered at $\theta = 1.914^\circ$, along with two small shoulder peaks around 1.88° and 1.95° . From the resonance condition diagram shown in Fig. 7 and the expected *apparent* width, the broad peak due to the $1s_{1/2} \rightarrow 2p_{3/2}$ transition covers the entire region, and the sharp peaks due to the transitions to the $n = 3$ level are also involved in this structure.

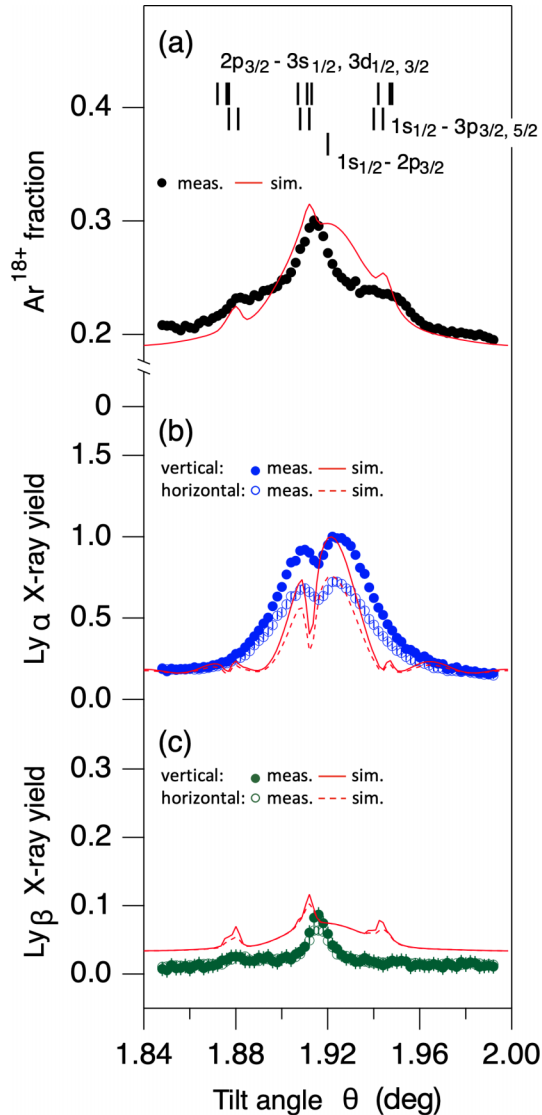


FIG. 8. Resonance profiles as a function of θ for 389.80 MeV/u Ar^{17+} at $\phi = -0.100^\circ$. (a) the Ar^{18+} fraction, (b) the $\text{Ly}\alpha$ x-ray yield, and (c) the $\text{Ly}\beta$ x-ray yield. The red curve overlaid on each profile is the corresponding resonance spectra from the simulation. Filled and open circles in the x-ray yield show measurements by the detector placed in the vertical and horizontal directions, respectively; corresponding resonance spectra from the simulation (solid and dashed red lines) are overlaid. For comparison between the experimental data and calculated results of x-ray yields, both are normalized to the largest intensity in the $\text{Ly}\alpha$ x-ray yield in the vertical direction.

These additional structures correspond to the transitions $2p_{3/2} \rightarrow 3d$ with the field specified by $\mathbf{g}_{0,8,m}$ or direct transition of $1s_{1/2} \rightarrow 3p_{1/2,3/2}$ with the field specified by $\mathbf{g}_{1,9,m}$, where $m = 2, 0, -2$. The sharp enhancements of ionization again reflect the larger ionization cross sections for the $n = 3$ level compared with the $n = 2$ level. Thus, the position of the observed central peak corresponds to the resonance condition to $3d$ states being shifted from $2p_{3/2}$, which is confirmed by the discussion below.

For the resonance profile of the $\text{Ly}\alpha$ x-ray yield emitted in both vertical and horizontal directions [Fig. 8(b)], we again observed a broad peak covering the entire scanning region

due to the $1s_{1/2} \rightarrow 2p_{3/2}$ transition. Angular anisotropy was also observed. A prominent feature is the dip at $\theta = 1.916^\circ$, slightly to the left of the center of the broad peak. The dip originates from the depletion of the $2p_{3/2}$ state population due to the $2p_{3/2} \rightarrow 3d_{3/2,5/2}$ transition. This characteristic feature is the smoking gun for population transfer by ladder-type DR. On either side of the dip in the $\text{Ly}\alpha$ x-ray profile, there is an expectation of the dip corresponding to the small shoulder peaks in the charge-state profile, but this is not so obvious. This might be related to the fact that the $2p_{3/2}$ state population at the tail of the broad resonance profile of the $1s_{1/2} \rightarrow 2p_{3/2}$ transition is not high, which is in contrast to the situation at the central region.

For the resonance profile of the $\text{Ly}\beta$ x-ray yield [Fig. 8(c)], we observed a sharp central peak at $\theta = 1.916^\circ$. This peak originates from the $3p_{1/2,3/2}$ states excited through V-type DR directly from the $1s_{1/2}$.

We again compare the observed resonance profiles with simulations. The calculated resonance profiles were overlaid in Fig. 8. For comparison between the experimental data and calculated results of x-ray yields, both are normalized to the largest intensity in the $\text{Ly}\alpha$ x-ray yield in the vertical direction. The overall agreement between the experimental results and the simulated profiles is reasonable. However, in Fig. 8(b), the simulated peak width is much narrower than the observation, and the characteristic reduction of the $\text{Ly}\alpha$ x-ray yield at the center of the broad peak was also clearly discernible by the narrow dip width in the simulation. This difference suggests that there are additional factors that are not included in the calculations but cause broadening. From the resonance width of the $1s \rightarrow 2p_{1/2}$ transition (not shown in this paper), we noticed a larger angular divergence of the beam under the experimental conditions for case II compared with case I, which is one of the sources of broadening. For the $\text{Ly}\beta$ x-ray yield, the structure of the main peak is well reproduced, although the predicted higher- and lower-energy side peaks are not clearly observed in the experiment. This is likely related to the broadening due to the angular divergence of the beam. In addition, the calculated background under the nonresonance conditions was found to be rather higher. We also noticed a slight difference in the dip position in the $\text{Ly}\alpha$ x-ray yield and the peak positions in the $\text{Ly}\beta$ x-ray yield between the experimental result and the simulation. The origin of these discrepancies has so far not been clarified. It is not attributed to problems in the calibration procedure of the tilt angle θ or errors in evaluating the incident ion energy. However, such discrepancies do not affect the discussion and conclusions.

Figure 9 shows the population evolution of each excited state as a function of the penetration depth from the entrance under the DR condition at $\theta = 1.912^\circ$. As in case I, the population of the $2p_{3/2}$ state grows, reaching a maximum at around $0.63 \mu\text{m}$ from the entrance and then decreases. The population of the $3d_{5/2}$ state increases due to population transfer from the $2p_{3/2}$ state and reaches as high as 13% at the exit. This is in contrast to the limited population growth in other states. In the approach of case II, the narrow *apparent* resonance width allows a cleaner extraction only ladder-type DR to the $3d_{5/2}$ state and minimizes the contribution of V-type DR to the $3p_{1/2,3/2}$ states.

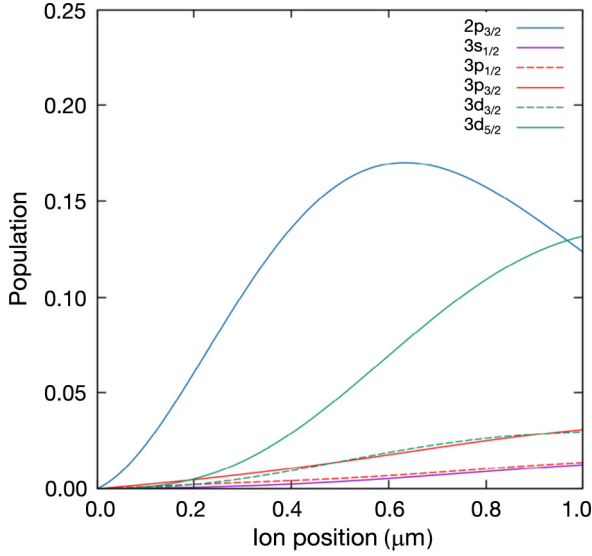


FIG. 9. Calculated evolution of the population of excited states of Ar^{17+} as a function of the penetration depth from the entrance in the crystal under the resonance condition of $\theta = 1.912^\circ$ and $\phi = -0.100^\circ$ for case II. The population is normalized to the incoming Ar^{17+} ions.

V. CONCLUSION

The $3d$ states of Ar^{17+} ions were produced by the 3D-RCE double-resonance (DR) technique via the ladder-type $1s_{1/2} \rightarrow 2p_{3/2} \rightarrow 3d_{3/2,5/2}$ transition. We obtained resonance profiles of the Ar^{18+} fraction, along with $\text{Ly}\alpha$ and $\text{Ly}\beta$ x-ray yields as a function of the transition energy by tilting the crystal angle. The $\text{Ly}\alpha$ x-ray yield provided solid evidence confirming the population transfer by ladder-type DR. Two different conditions were employed. Under the first condition (case I), the ladder-type DR was observed as the depletion of the resonance amplitude of the $\text{Ly}\alpha$ x-ray emission yield compared to the SR case of $1s_{1/2} \rightarrow 2p_{3/2}$ due to the population transfer of $2p_{3/2} \rightarrow 3d_{3/2,5/2}$ states. Under the second condition (case II), this depletion was observed more clearly owing to the narrow resonance, where the higher-order resonance by $\mathbf{g}_{k,l,m}$ with a large l component was employed for the $2p_{3/2} \rightarrow 3d_{3/2,5/2}$ transitions. These transitions were observed as a sharp dip in the broad resonance profile of the first excitation of $1s_{1/2} \rightarrow 2p_{3/2}$. Under these conditions, the V-type DR of $1s_{1/2} \rightarrow 2p_{3/2}$ and $1s_{1/2} \rightarrow 3p_{1/2,3/2}$ transitions also occur. Theoretical calculations using the density matrix method indicate that ladder-type DR can be chosen more selectively than V-type DR, taking advantage of the narrow *apparent* resonance width in case II.

By combining two crystal fields equivalent to two different x rays, we succeeded in demonstrating the efficient production of $3d$ states in H-like heavy ions up to more than 10% in which the transition from the $1s_{1/2}$ ground state is optically forbidden. This method is also a promising tool for sequential excitation into optically forbidden higher excited states. Preliminary resonance profiles have been observed for $n = 4$ and 5 excitations.

ACKNOWLEDGMENTS

The authors acknowledge Professor V. V. Balashov (deceased), and A. A. Sokolik for helpful discussions on the theoretical calculations. This experiment was one of the research projects with heavy ions at NIRS-HIMAC, and performed at the beam time in 2013-2015. This work was supported by JSPS KAKENHI Grants No. 26220607, No. 26287141, and No. 22KK0037, and the RIKEN Pioneering Projects.

APPENDIX: ANISOTROPIC ANGULAR DISTRIBUTION OF X-RAY EMISSION

A theoretical treatment of the anisotropic angular distribution of x-ray emission was already described elsewhere [26]. Hereafter, a brief summary related to the present experiment is explained. Concerning x-ray emission from the excited states, we discuss the observed ratio of x-ray yields in the vertical and horizontal directions. By the Lorentz transformation of the crystal potential, the polarization direction of the oscillating electric field in the ion rest frame is found to be parallel to $(\gamma g_x, \gamma g_y, g_z)$. Reflecting the character of electric dipole radiation in the geometric layout of the present experiment, the x-ray detector placed in the vertical plane detected x rays from the $2p_y, 2p_z$ or $3p_y, 3p_z$ substates. The horizontal detector observed deexcitation of the $2p_x, 2p_z$ or $3p_x, 3p_z$ substates.

In the presence of an internal perturbation to the excited state by the spin-orbit interaction, the excited states undergo a time modulation of alignment parameters during the time between excitation and radiative decay. The period of the modulation determined by the fine-structure splitting is 8.6×10^{-16} s for the $n = 2$ level of H-like Ar^{17+} , which is much shorter than the lifetime of the excited state. In such conditions, the time integration of the alignment parameters over the period can be considered. The angular distribution of the electric dipole radiation from the perturbed system is given by

$$I(\xi) = \frac{1}{2}(1 - c_2 \cos 2\xi), \quad (\text{A1})$$

where ξ is the angle from the polarization direction and c_2 ($0 \leq c_2 \leq 1$) is the shape parameter denoting the degree of linear polarization. A decrease in c_2 means the loss of polarization: $c_2 = 1$ gives the pure dipole radiation pattern of $\sin^2 \xi$, and $c_2 = 0$ gives a completely isotropic radiation pattern. The shape parameter can be obtained analytically using the density matrix description. For the $2p_{1/2} \rightarrow 1s$ and $2p_{3/2} \rightarrow 1s$ transitions, $c_2 = 0$ and $3/5$, respectively [27]. Therefore, anisotropy is absent in the radiation from $2p_{1/2}$, while radiation from the $2p_{3/2}$ state shows an anisotropic angular distribution with respect to the polarization direction, although it is affected by the spin-orbit interaction.

The theoretical V/H ratio, $R_{V/H}$, is given by $I(\xi_x)/I(\xi_y)$. In the present experimental configuration

$$\begin{aligned} \cos \xi_x &= \frac{|\mathbf{F}'_{\mathbf{g}_x}|}{|\mathbf{F}'_{\mathbf{g}}|} = \frac{\gamma |g_x|}{\sqrt{\gamma^2 (g_x^2 + g_y^2) + g_z^2}}, \\ \cos \xi_y &= \frac{|\mathbf{F}'_{\mathbf{g}_y}|}{|\mathbf{F}'_{\mathbf{g}}|} = \frac{\gamma |g_y|}{\sqrt{\gamma^2 (g_x^2 + g_y^2) + g_z^2}}. \end{aligned} \quad (\text{A2})$$

The $R_{V/H}$ from the $2p_{3/2}$ state is

$$R_{V/H} = \frac{4 - 3 \cos^2 \xi_x}{4 - 3 \cos^2 \xi_y}. \quad (\text{A3})$$

-
- [1] S. Kühn, C. Cheung, N. S. Oreshkina, R. Steinbrügge, M. Togawa, S. Bernitt, L. Berger, J. Buck, M. Hoesch, J. Seltmann *et al.*, *Phys. Rev. Lett.* **129**, 245001 (2022).
- [2] E. Ferrari, C. Spezzani, F. Fortuna, R. Delaunay, F. Vidal, I. Nikolov, P. Cinquegrana, B. Diviacco, D. Gauthier, G. Penco *et al.*, *Nat. Commun.* **7**, 10343 (2016).
- [3] A. Picón, C. S. Lehmann, C. Bostedt, A. Rudenko, A. Marinelli, T. Osipov, D. Rolles, N. Berrah, C. Bomme, M. Bucher, G. Doumy *et al.*, *Nat. Commun.* **7**, 11652 (2016).
- [4] I. Inoue, Y. Inubushi, T. Sato, K. Tono, T. Katayama, T. Kameshima, K. Ogawa, T. Togashi, S. Owada, Y. Amemiya *et al.*, *Proc. Natl. Acad. Sci. USA* **113**, 1492 (2016).
- [5] E. Prat, P. Dijkstal, E. Ferrari, R. Ganter, P. Juranić, A. Malyzhenkov, S. Reiche, T. Schietinger, G. Wang, A. A. Haddad *et al.*, *Phys. Rev. Res.* **4**, L022025 (2022).
- [6] D. Budker, J. R. C. López-Urrutia, A. Derevianko, V. V. Flambaum, M. W. Krasny, A. Petrenko, S. Pustelny, A. Surzhykov, V. A. Yerokhin, and M. Zolotarev, *Ann. Phys. (Leipzig)* **532**, 2000204 (2020).
- [7] K. Komaki, T. Azuma, T. Ito, Y. Takabayashi, Y. Yamazaki, M. Sano, M. Torikoshi, A. Kitagawa, E. Takada, and T. Murakami, *Nucl. Instrum. Methods Phys. Res., Sect. B* **146**, 19 (1998).
- [8] T. Azuma, T. Ito, K. Komaki, Y. Yamazaki, M. Sano, M. Torikoshi, A. Kitagawa, E. Takada, and T. Murakami, *Phys. Rev. Lett.* **83**, 528 (1999).
- [9] C. Kondo, S. Masugi, Y. Nakano, A. Hatakeyama, T. Azuma, K. Komaki, Y. Yamazaki, T. Murakami, and E. Takada, *Phys. Rev. Lett.* **97**, 135503 (2006).
- [10] Y. Nakano, C. Kondo, A. Hatakeyama, Y. Nakai, T. Azuma, K. Komaki, Y. Yamazaki, E. Takada, and T. Murakami, *Phys. Rev. Lett.* **102**, 085502 (2009).
- [11] Y. Nakai, Y. Nakano, T. Azuma, A. Hatakeyama, C. Kondo, K. Komaki, Y. Yamazaki, E. Takada, and T. Murakami, *Phys. Rev. Lett.* **101**, 113201 (2008).
- [12] Y. Nakano, S. Suda, A. Hatakeyama, Y. Nakai, K. Komaki, E. Takada, T. Murakami, and T. Azuma, *Phys. Rev. A* **85**, 020701(R) (2012).
- [13] Y. Nakano, A. A. Sokolik, A. V. Stysin, Y. Nakai, K. Komaki, E. Takada, T. Murakami, and T. Azuma, *J. Phys. B: At., Mol. Opt. Phys.* **48**, 144026 (2015).
- [14] V. V. Okorokov, *JETP Lett.* **2**, 111 (1965).
- [15] S. Datz, C. D. Moak, O. H. Crawford, H. F. Krause, P. F. Dittner, J. Gomez del Campo, J. A. Biggerstaff, P. D. Miller, P. Hvelplund, and H. Knudsen, *Phys. Rev. Lett.* **40**, 843 (1978).
- [16] H. Bethe and E. E. Salpeter, *Quantum Mechanics of One- and Two-Electron Systems* (Springer, New York, 1957).
- [17] O. Jitrik and C. F. Bunge, *J. Phys. Chem. Ref. Data* **33**, 1059 (2004).
- [18] The NIST database: <https://www.nist.gov/pml/atomic-spectra-database>.
- [19] H. F. Krause, S. Datz, P. F. Dittner, N. L. Jones, and C. R. Vane, *Phys. Rev. Lett.* **71**, 348 (1993).
- [20] V. V. Balashov, A. A. Sokolik, and A. V. Stysin, *J. Exp. Theor. Phys.* **108**, 1010 (2009).
- [21] V. V. Balashov and I. V. Bodrenko, *Nucl. Instrum. Methods Phys. Res., Sect. B* **245**, 52 (2006).
- [22] V. V. Balashov and A. A. Sokolik, *Opt. Spectrosc.* **103**, 761 (2007).
- [23] V. V. Balashov and A. A. Sokolik, *J. Exp. Theor. Phys.* **107**, 133 (2008).
- [24] H. F. Beyer, H.-J. Kluge, and V. P. Shevelko, *X-Ray Radiation of Highly Charged Ions* (Springer, Berlin, Heidelberg, 1997).
- [25] E. Lamour, P. D. Fainstein, M. Galassi, C. Prigent, C. A. Ramirez, R. D. Rivarola, J.-P. Rozet, M. Trassinelli, and D. Vernhet, *Phys. Rev. A* **92**, 042703 (2015).
- [26] Y. Nakano, A. Hatakeyama, Y. Nakai, K. Komaki, E. Takada, T. Murakami, and T. Azuma, *Phys. Scr.* **T156**, 014061 (2013).
- [27] N. Andersen and K. Bartschat, *Polarization, Alignment, and Orientation in Atomic Collisions* (Springer, New York, 2001).